Quantum Electronic Structure

Embedded Mean-Field Theory for Solution-Phase Transition-Metal Polyolefin Catalysis

Leanne D Chen, James Joseph Lawniczak, Feizhi Ding, Peter J. Bygrave, Saleh Riahi, Frederick R. Manby, Sukrit Mukhopadhyay, and Thomas Francis Miller

J. Chem. Theory Comput., **Just Accepted Manuscript** • DOI: 10.1021/acs.jctc.0c00169 • Publication Date (Web): 22 May 2020

Embedded Mean-Field Theory for Solution-Phase Transition-Metal Polyolefin Catalysis

Leanne D. Chen,[†] James J. Lawniczak,[†] Feizhi Ding,[†] Peter J. Bygrave,[‡] Saleh Riahi,[†] Frederick R. Manby,[‡] Sukrit Mukhopadhyay,[¶] and Thomas F. Miller III[*,†]

[†]*Division of Chemistry and Chemical Engineering, California Institute of Technology, Pasadena, CA 91125, USA*

[‡]*Centre for Computational Chemistry, University of Bristol, Bristol BS8 1TS, United Kingdom*

[¶]*The Dow Chemical Company, Midland, MI 48674, USA*

E-mail: tfm@caltech.edu

Abstract

Decreasing the wall-clock time of quantum mechanics/molecular mechanics (QM/MM) calculations without sacrificing accuracy is a crucial prerequisite for widespread simulation of solution-phase dynamical processes. In this work, we demonstrate the use of embedded mean-field theory (EMFT) as the QM engine in QM/MM molecular dynamics (MD) simulations to examine polyolefin catalysts in solution. We show that employing EMFT in this mode preserves the accuracy of hybrid-functional DFT in the QM region, while providing up to 20-fold reductions in the cost per SCF cycle, thereby increasing the accessible simulation time-scales. We find that EMFT reproduces DFT-computed binding energies and optimized bond lengths to within chemical

accuracy, as well as consistently ranking conformer stability. Furthermore, solution-phase EMFT/MM simulations provide insight into the interaction strength of strongly coordinating and bulky counterions.

Introduction

Catalyst design in transition-metal catalysis typically requires extensive experimental optimization to achieve desired product characteristics.[1] Efficient catalysts – many of which have complex ligand structures – are often difficult and expensive to synthesize. To circumvent the bottleneck this presents in research and development efforts, advances in computational methods can help accelerate the identification of promising ligands.[2] *De novo* catalyst design is challenging due to the subtle interplay of electronic and steric effects on the performance of the catalyst under specific reaction conditions. Further complicating catalyst design are the important effects of solvent, conformational flexibility, and counterions at finite temperature and concentration.[3] New methods are needed to provide reliable computational insight into the effective design of catalysts in their solvation environment.

The combined quantum mechanics/molecular mechanics (QM/MM) method[4,5] has proven effective in a variety of applications including biological reactions[6–11] and solution-phase chemistry,[12–16] due to its ability to address both dynamical effects in multi-scale systems along with local bond-making and bond-breaking events. The cost of a single QM/MM MD step is usually dominated by that of the force evaluation for the QM region, since the MM interactions have a simple analytic form. Therefore, managing the cost of the QM calculation is an important objective for the development of computationally efficient solution-phase QM/MM simulations.

Quantum embedding offers an appealing strategy for reducing the computational costs associated with the QM regions while preserving its accuracy. For example, wavefunction-in-(density functional theory) quantum embedding methods[17–20] provide high (i.e., coupled-cluster theory) accuracy in the QM region at a significant reduction in cost versus a full wavefunction-method description,[21,22] although this approach remains too costly for widespread use in QM/MM MD simulations.

In the current work, we employ an alternative quantum embedding approach in the QM region, specifically embedded mean-field theory (EMFT),[23,24] which provides a high-quality

mean-field description (such as DFT with a hybrid functional using a large atomic-orbital basis set) for a subsystem of the QM region, while the remainder of the QM region is described using a less costly mean-field method (such as DFT with a GGA functional using a small atomic-orbital basis set). A key advantage of the method is that it does not require specification of link atoms that connect the subsystems, nor does it require specification of the number of subsystem spin states or the number of electrons per subsystem. Previous work has shown that EMFT can be much more accurate than both the point-charge[25] and ONIOM[26,27] schemes for subsystem embedding, particularly for systems that involve partitioning across delocalized covalent bonds.[23,28] EMFT has additionally been benchmarked for open-shell systems,[23] for deprotonation reactions,[29] and for the linear-response description of excited states.[30] As we will show, this leads to tangible advances in terms of the information we can glean in the application area we study.

Polyolefins are the most widely used class of polymers[31] whose industrial importance is in part due to the tunability of their mechanical and physical properties, such as elasticity and opacity. Precise control of these macroscopic properties requires an atomic-scale mapping of the barriers of the elementary steps in the polymerization mechanism (Figure 1),[32] where the goal is to design molecular catalysts that offer superior control of product selectivity over their heterogeneous analogues.[33] Nuclear magnetic resonance (NMR) studies have suggested that configurational sampling of the solvent and counterion degrees of freedom near the catalyst play a crucial role in its functionality,[34] which necessitates the application of dynamic rather than static modeling techniques. A chemically accurate description of the electronic structure near the active site is necessary to reliably describe reactivity at the active site. For these reasons, QM/MM studies have typically been used to study transition-metal catalysts in solution.[35–40] In this work, we show that replacing DFT with EMFT for the QM subsystem in these solution-phase QM/MM simulations of organometallic compounds largely preserves the accuracy of the description for these organometallic compounds while substantially improving computational efficiency.

The current work focuses on four archetypal Group (IV) molecular catalysts for olefin polymerization (Figure 2), which include both metallocene and post-metallocene structures. Catalyst 1 is a constrained geometry complex (CGC) of the metallocene class of polyolefin catalysts.[41,42] Catalyst 2 is a post-metallocene structure, where the reaction of interest in this case is the binding of propylene to the Hf^{4+} active site.[43] The competition between the binding of ethylene and propylene in the polymerization process influences the branching ratio in the final product, which influences its bulk material properties. Catalyst 3 and Catalyst 4 are also post-metallocene structures, which have been previously reported to produce olefin block copolymers with favorable elastomeric properties.[44] (The full chemical names of the catalysts are provided in the Supporting Information.)

Computational Methods

Density functional theory (DFT) is widely used for *ab initio* simulations because of its balance between accuracy and computational cost. For organometallic compounds in particular,[45–48] various DFT studies have demonstrated the importance of using hybrid exchange correlation functionals[49–52] which include some fraction of exact Hartree-Fock exchange, although such hybrid functionals are typically more computationally expensive than those that employ the generalized gradient approximation (GGA) alone.[53] Embedded mean-field theory (EMFT)[23,24] seeks the best of these two worlds — hybrid functional-like predictions at a computational cost similar to that of the GGA, yielding experimentally relevant quantities with chemical accuracy.[28] EMFT is a simple, self-consistent method that provides a high-level DFT (or other mean-field) description on a subset of the system and a lower-level DFT (or other mean-field) description on the remainder.[23]

All DFT and EMFT calculations reported here are performed using the *entos* package.[54] For the B3LYP functional used in the paper, the VWN3 local correlation energy[55] is employed. We employ the density-corrected implementation of the method (DC-EMFT) to

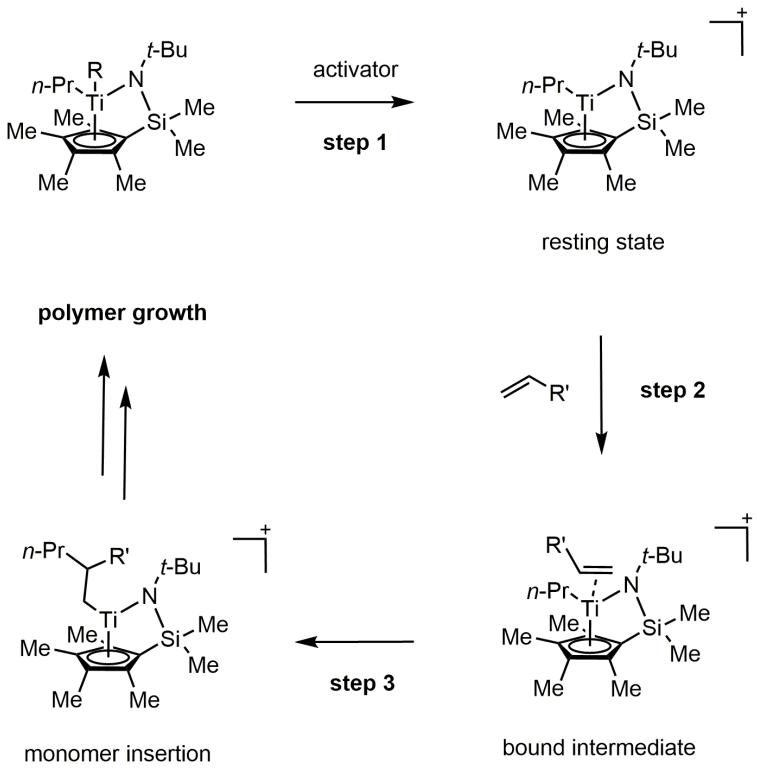

Figure 1: Initial steps leading up to the catalytic cycle of a Group (IV) metal-catalyzed olefin polymerization, including abstraction of an alkyl group (represented as R) by an oxidizing activator reagent to form the catalytically-active resting state (Step 1), binding of the first monomer to the resting state species (Step 2), and insertion of bound monomer into the initial alkyl (here, *n*-propyl) ligand (Step 3). Afterwards, monomer binding and insertion into the growing polymer chain repeat until termination.

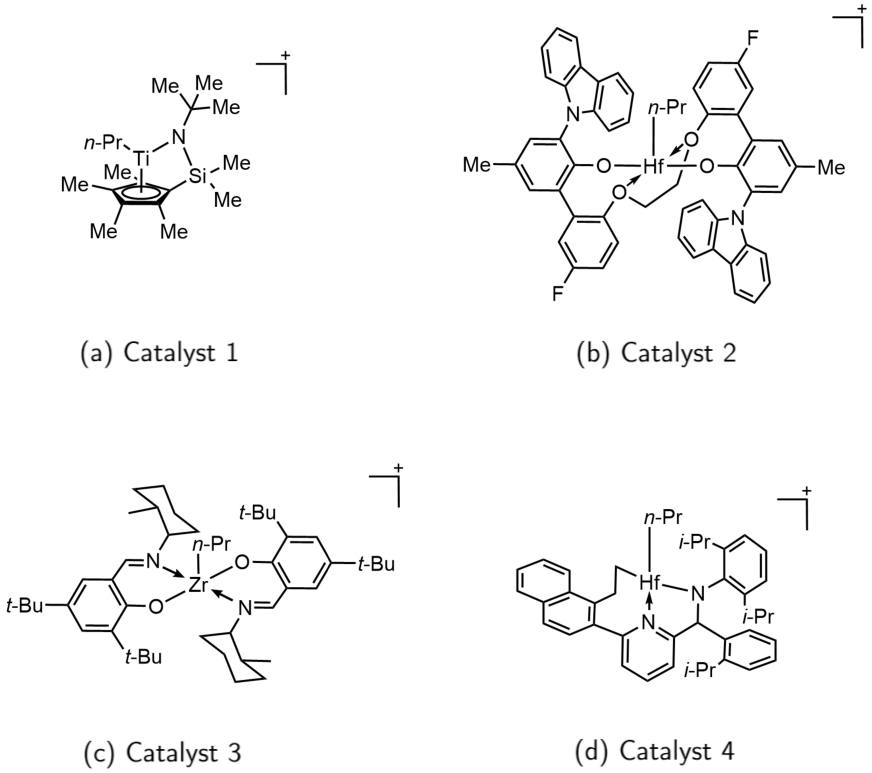

(a) Catalyst 1 (b) Catalyst 2

(c) Catalyst 3 (d) Catalyst 4

Figure 2: Transition-metal polyolefin catalysts considered here (resting state depicted). (**a**) Catalyst 1 is a metallocene complex belonging to the constrained geometry complex (CGC) class. (**b**) Catalyst 2 is a post-metallocene catalyst containing bisphenol ligands. (**c**) Catalyst 3 is a post-metallocene FI-type catalyst containing Schiff base amines. (**d**) Catalyst 4 is a post-metallocene catalyst with a pyridyl-amido motif.

prevent unphysical collapse of the electronic density.[24] The exact-exchange contributions to the coupling between the high- and low-level subsystems are treated using the EX0 scheme.[23] For the predictions of catalyst conformer stability, configurational sampling was performed using thermostatted molecular dynamics on the GFN1-xTB[56] potential using the *entos* package.[54] A linear cooling schedule from 800 K to 100 K was used, with a total sampling time of 70 ps and time step of 1 fs. Sampled configurations were subsequently optimized using (B3LYP/Def2-SVP).

QM/MM simulations are carried out by interfacing *entos*[54] with the GROMACS 2018.1 molecular dynamics software.[57] The toluene solvent is described using the modification of the OPLS-AA[58] force-field by Caleman and coworkers,[59,60] and σ and ϵ values for the titanium atom are taken from Cu^{2+} in the OPLS-AA database. Partial charges of the metal complex are obtained from Mulliken population analysis[61] performed on the complex using (B3LYP/Def2-SVP). The force-field parameters for borate counterions, including methyl [tris(pentafluorophenyl)]borate, tetrakis(pentafluorophenyl)borate, and BF_4^-, are obtained from a previous study.[62] GROMACS parameter and topology files employed in this study are provided in the Supporting Information.

QM/MM simulations are carried out with electrostatic interactions calculated using the reaction-field-zero method.[63] The charge-group cutoff scheme is used, with the solvent molecules comprised of neutral charge groups and with the catalyst and counterion comprised of charge groups with net charges. Electrostatic coupling between the QM and MM particles is evaluated through the electrostatic embedding scheme. Other non-bonded interactions between the QM and MM particles are calculated using the Lennard-Jones potential with parameters provided in the Supporting Information.

All covalent bonds in the solvent and counteranion structures are constrained using the LINCS algorithm.[64] The leap-frog integrator is used with a 1 fs time step. Periodic boundary conditions (PBCs) are used, with a 1.2 nm cutoff for electrostatic and vdW interactions. The electrostatic cutoff is applied with respect to the distance between the geometrical (i.e., un-

mass weighted) centers of the charge groups. When employed, the Nosé-Hoover thermostat[65] and the Parrinello-Rahman barostat[66] are utilized with a temperature of 298 K, a pressure of 1 bar, and a damping time constant of 1 ps.

The initial configurations for the QM/MM simulations are prepared as follows: The solvated catalyst and counterion were initialized from a pre-equilibrated simulation cell, obtained using the `solvate` utility within the GROMACS package,[67] and performing a 1 ns isothermal-isobaric (NpT) equilibration using fully classical MD. For the Cl^-, BF_4^-, $CH_3B(C_6F_5)_3^-$ and $B(C_6F_5)_4^-$ simulations, the number of solvent molecules is respectively 196, 196, 193, and 195. During this initial equilibration, the cubic simulation cell adopts a sidelength of approximately 3.3 nm centered around the catalyst. The system was then equilibrated for 5 ps in the NpT ensemble using the GFN1-xTB/MM potential, then for at least 5 ps in the NVT ensemble using the EMFT/MM potential, before performing production runs in the NVE ensemble using the EMFT/MM potential. Each QM/MM production run has a simulation time of at least 30 ps.

Results and Discussion

Benchmarking EMFT Accuracy and Cost

We begin by benchmarking the accuracy and efficiency of EMFT for the prediction of structure and reactivity of the archetypal Group (IV) olefin polymerization catalysts shown in Figure 2. In particular, we focus on monomer binding energies, resting-state bond lengths, and relative-energy rankings of a resting-state conformer using EMFT.

For DFT calculations, we specify the exchange correlation functional and basis set with the standard nomenclature (functional/basis set). For EMFT, we specify the level of theory via ((high-level)-in-(low-level)); for example, ((B3LYP/Def2-SVP)-in-(PBE/6-31G)) denotes the use of EMFT with the B3LYP functional and Def2-SVP basis for the high-level subsystem and the PBE functional and 6-31G basis for the low-level subsystem.

Substrate binding energies

The binding of a monomer substrate is an important elementary step in the overall polymerization mechanism (Figure 1). We compare the binding energy values obtained by EMFT ((B3LYP/Def2-SVP)-in-(PBE/6-31G)) to those calculated using high-level DFT (B3LYP/Def2-SVP) and low-level DFT (PBE/6-31G). Additionally, we investigate the convergence of EMFT binding energy values to the high-level DFT result, as a function of high-level subsystem size. To calculate the binding energy using DFT or EMFT, we take the difference between the single-point energies of the bound intermediate product and the resting state and unbound ethylene reactants (Step 2, Figure 1). The unbound ethylene monomer is treated with (B3LYP/Def2-SVP) for EMFT and high-level DFT, and with (PBE/6-31G) for low-level DFT. All calculations are performed at geometries that are optimized at the B3LYP level of theory; these structures for both the resting-state and substrate-bound intermediates for all four catalysts are provided in the Supporting Information.

For EMFT energy evaluations of the resting state and bound intermediate catalyst structures, the partitioning of the system is illustrated in Figure 3 and Figure 4. For each catalyst, four subsystem sizes are explored using EMFT. To compactly label the high-level regions for each subsystem size, we assign each atom a label from 1–4 in the resting state structure of the catalyst (Figure 3), with hydrogen atoms atoms sharing the index of the heavy atom to which they are bonded. Hence, a partitioning scheme $X \in \{1, 2, 3, 4\}$ defines the high-level subsystem as all atoms which have an index value less than or equal to X. For example, partitioning scheme 2 places both the blue (label 1) and green (label 2) atoms in the high-level subsystem. The atomic labelling for the resting states as shown in Figure 3 extend to the bound intermediate; as shown in Figure 4, the monomer substrate in the unbound and bound intermediate structure is always included in the high-level subsystem.

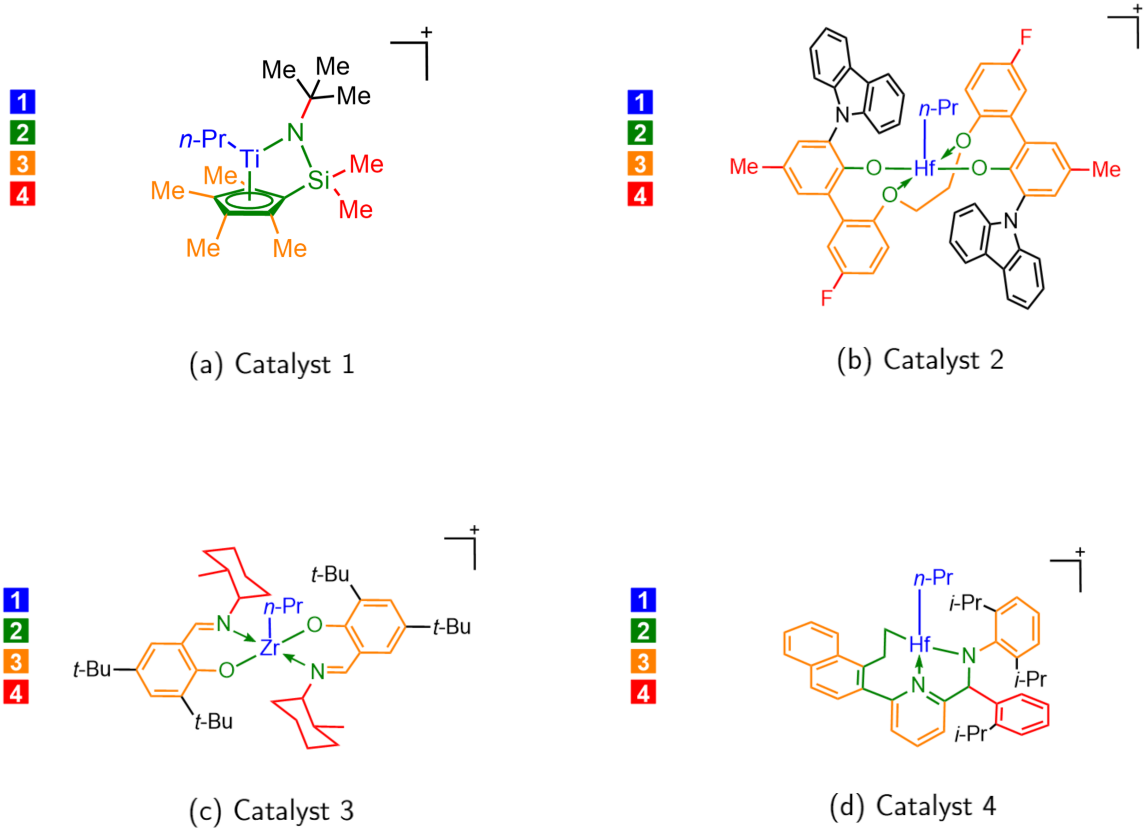

(a) Catalyst 1 (b) Catalyst 2

(c) Catalyst 3 (d) Catalyst 4

Figure 3: Definition of the high-level subsystem by atomic labeling (shown for resting state structures) for EMFT partitioning. For a partitioning scheme X indexed as 1, 2, 3, 4, the atoms with indices of less than or equal to X are in the high-level region, and the remaining atoms are in the low-level region; moieties indicated in black are in all cases treated at the low level. For each atom that is joined by bonds containing different colors, the label corresponding to the lower index is used. All implicit hydrogen atoms share the index of the atom to which they are bonded. For example, partitioning scheme 2 places the blue- and green-labeled atoms in the high-level subsystem, and the remaining atoms in the low-level subsystem.

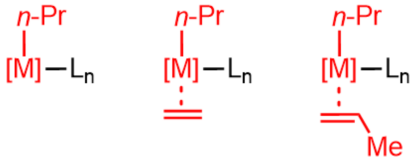

Figure 4: Illustration of the partitioning for the minimal high-level subsystem (Figure 3, $X = 1$) for the resting state, ethylene-bound intermediate, and propylene-bound intermediate, respectively. The high-level subsystem (represented in red) always contains at least the metal, *n*-propyl group, and if present in the structure, the bound monomer.

Binding energies for ethylene (black dots) and propylene (gray dots) are plotted as a function of the number of atoms in the high-level subsystem (Figure 5). All binding energies are reported relative to the ethylene binding energy calculated by low-level DFT (PBE/6-31G). On each plot, the first point corresponding to zero atoms in the high-level subsystem is obtained from the low-level DFT (PBE/6-31G) energy, and the last point corresponding to the inclusion of all atoms in the high-level subsystem is obtained from the high-level (B3LYP/Def2-SVP) energy. The four intermediate points indicate the EMFT energy calculated using increasing sizes of the high-level subsystem. To indicate the target range of chemical accuracy, the light and dark green bar indicates ± 1 kcal/mol deviation from the high-level DFT (B3LYP/Def2-SVP) propylene and ethylene binding energy, respectively.

EMFT-calculated ethylene and propylene energies converge to the high-level DFT result for all four catalysts (Figure 5). For all four of the catalyst systems, the minimal subsystem – including the growing polymer chain, the metal center, and the unbound or bound monomer – is sufficient to obtain the energy of ethylene and propylene binding to within $\sim$1 kcal mol^{-1} of the high-level calculation on the full system. For some intermediate subsystem sizes, the error is slightly larger than 1 kcal mol^{-1}, but in general the deviations are modest. Notably, this effect holds for large catalysts, including the largest catalyst studied (Catalyst 3, with 127 atoms in the resting state form), for which the computational speed-ups will be greatest using EMFT. It is particularly encouraging that EMFT consistently provides good accuracy

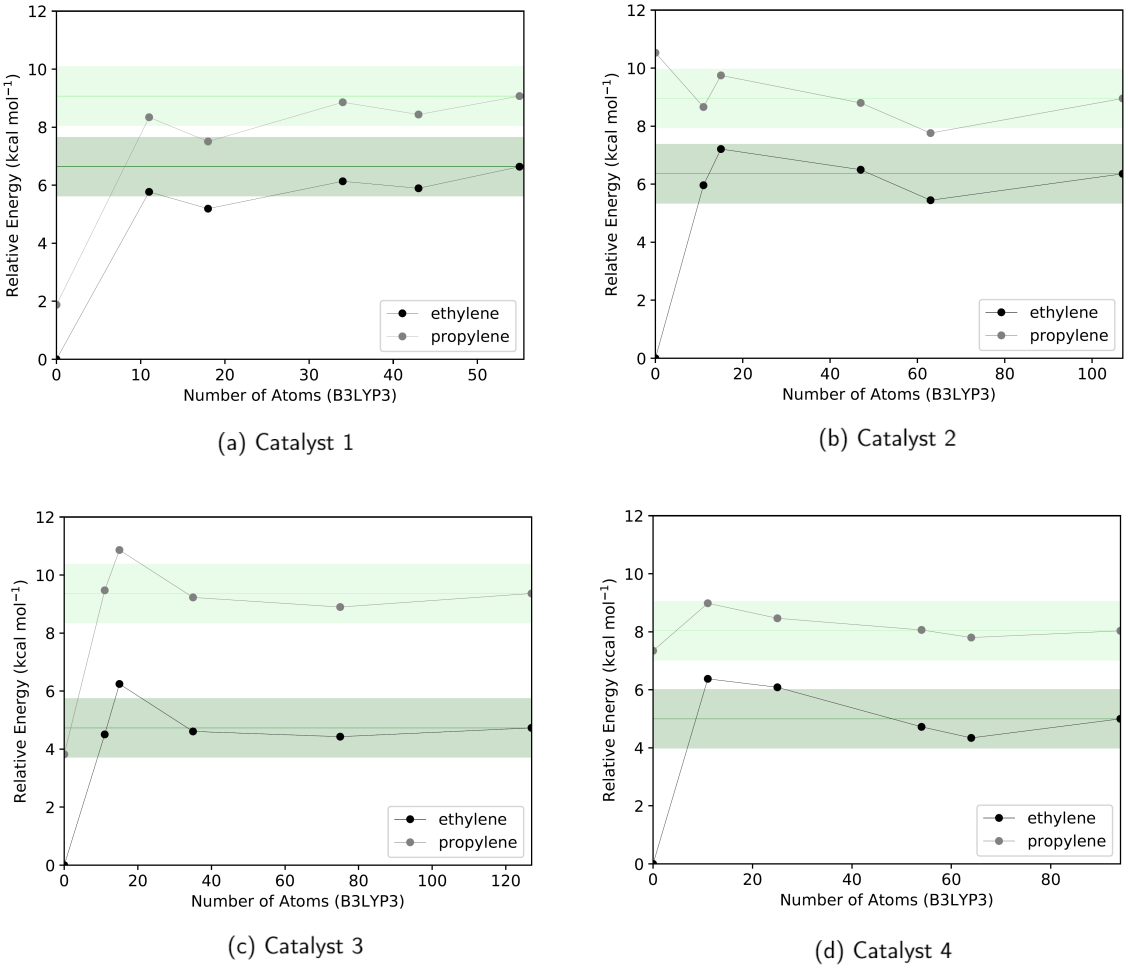

Figure 5: Ethylene and propylene binding energies relative to the low-level calculated ethylene binding energy (PBE/6-31G), as a function of the number of atoms in the high-level subsystem of the resting state structure. On each plot, from left to right is shown the full low-level DFT (PBE/6-31G), EMFT ((B3LYP/Def2-SVP)-in-(PBE/6-31G)) using partitioning schemes in Figure 3, and full high-level DFT (B3LYP/Def2-SVP). The number of atoms in each case coincide with the subsystem partitionings indicated in Figure 3.

across all four catalyst systems, which vary with respect to the transition metal and ligand scaffold.

Figure 6 addresses the accuracy with which EMFT predicts the relative binding energy of ethylene versus propylene in the four catalyst systems, a quantity that is of central interest in determining selectivity with respect to unwanted side-products during polyolefin catalysis. In all four cases, EMFT is performed using the smallest and least computationally expensive high-level subsystem considered (partitioning scheme 1). Comparing these EMFT results with respect to high-level DFT, it is clear that the lower-cost EMFT method accurately predicts ethylene and propylene binding energies across all four catalysts.

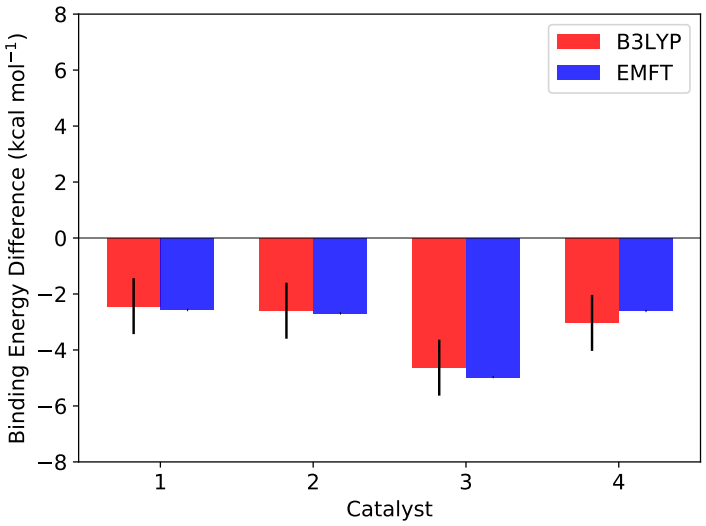

Figure 6: Difference in ethylene vs. propylene binding energy (ethylene – propylene) for Catalyst 1 (Ti^{4+}), Catalyst 2 (Hf^{4+}), Catalyst 3 (Zr^{4+}), and Catalyst 4 (Hf^{4+}). The differences in binding energies is evaluated with both DFT (B3LYP/Def2-SVP) and EMFT ((B3LYP/Def2-SVP)-in-(PBE/6-31G)) using the minimal subsystem partitioning (Figure 3, $X = 1$). A 1 kcal mol^{-1} error bar is included for comparing the DFT and EMFT binding energy differences.

Predicting conformer stability

An important capability in computational screening is the ability to predict the structure and relative energy of the most stable conformers. We investigate the distribution of con-

formers for resting state of Catalyst 3, which consists of a trigonal bipyramidal geometry with 2 oxygen ligands, 2 nitrogen ligands, and an n-propyl ligand. Three unique isomers are considered (Isomers 1–3, Figure 7), based on the orientation of the bonding connectivity at the metal site. We consider four low-energy conformers associated with each isomer, obtained via simulated annealing (see Computational Methods). Specifically, an independent simulated annealing trajectory was performed for each of the three isomers of Catalyst 3, and from each trajectory, the four lowest-energy distinct structures that were obtained after local minimization using high-level DFT (B3LYP/Def2-SVP) were included in this analysis. All structures are provided in the Supporting Information. For all calculations reported in this section, ((B3LYP/Def2-SVP)-in-(PBE/6-31G)) EMFT is performed using the smallest and least computationally expensive high-level subsystem considered (partitioning scheme 1).

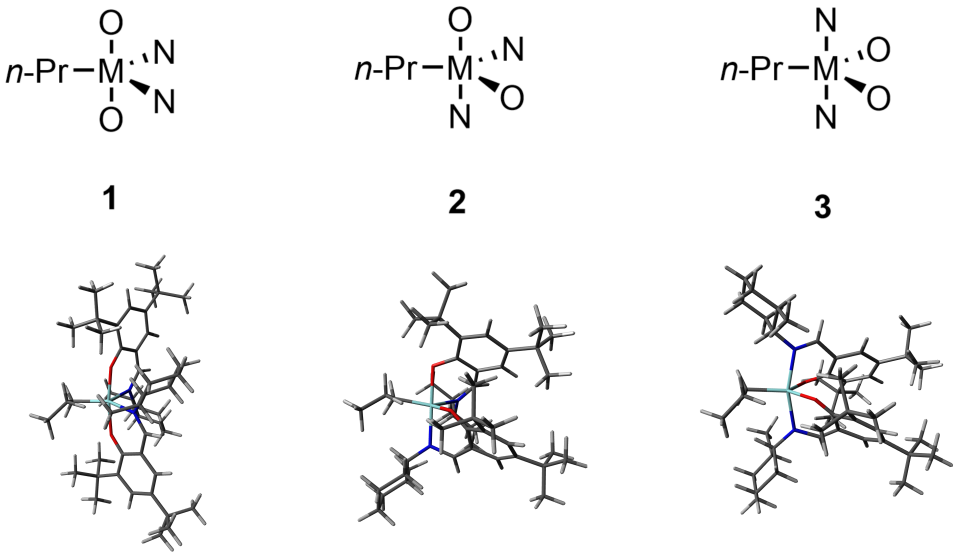

Figure 7: Three isomers of the Catalyst 3 resting state. Isomers 1–3 are displayed above, with different arrangements of the nitrogen- and oxygen-based ligands at the axial and equatorial sites. The *n*-propyl ligand is held at the equatorial position in all cases.

Figure 8a presents the correlation between the relative conformer energies computed using high-level DFT versus EMFT, for structures optimized using high-level DFT. As is clear from the plot, the prediction of conformer energy rankings from EMFT is excellent, with the rank-ordering of the 12 conformers – including those across isomers and with a given isomer – being correctly predicted using EMFT. We further note that the overall R^2 value of the correlation is 0.994, and that for every structure except the highest energy one, the EMFT relative energy predictions coincide with the high-level DFT prediction to within 1 kcal/mol (indicated by the shaded region).

Figure 8b then tests the degree to which the optimization of the geometries using EMFT (versus high-level DFT) effects the quality of the conformer energy ranking. Each of the twelve conformer structures that were initially optimized using high-level DFT were subsequently optimized using EMFT, and the energy of high-level DFT energy (at the high-level DFT optimized geometry) is correlated against the EMFT energy (at the EMFT optimized geometry). For all cases the error between the DFT and EMFT energy is less than 2

kcal/mol. The correlation remains excellent ($R^2 = 0.997$), and the relative ranking of the conformer remains perfect (with the exception of two nearly iso-energetic conformers of isomer 2). These results suggest that EMFT provides a powerful tool for screening catalyst conformers, without the need for high-level DFT geometries or even single-point energies.

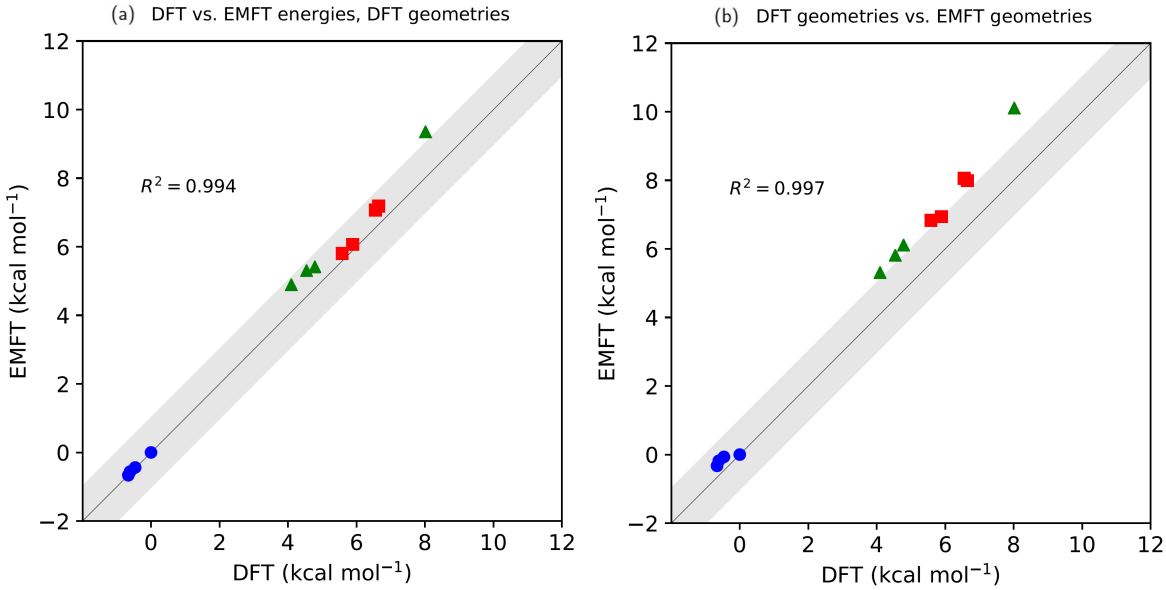

Figure 8: Comparison of DFT and EMFT energy rankings of the 12 conformers obtained by simulated annealing. The blue circles correspond to conformers of Isomer 1, the red squares to those of Isomer 2, and the green triangles to those of Isomer 3. The gray bar represents a 1 kcal mol^{-1} error bar at the diagonal. (**a**) DFT vs. EMFT energy for DFT-optimized conformer geometries. (**b**) DFT energy of DFT-optimized conformer geometries vs. the EMFT energy of the EMFT-optimized conformer geometries.

Predicted geometries

From an energy perspective, Figure 8b indicates that EMFT provides a satisfactory description of the optimized geometry for the catalyst resting state, which tends to be the most abundant species in catalytic mechanism.[68] We now further investigate the quality of the EMFT-optimized structures for the catalyst resting state across all Catalysts 1-4. For each resting state structure of the catalysts, geometry optimization was performed with high-level DFT (B3LYP/Def2-SVP), EMFT ((B3LYP/Def2-SVP)-in-(PBE/6-31G)), using

the minimal partitioning scheme 1, and low-level DFT (PBE/6-31G).

For Catalyst 1, Table 1 presents representative bond lengths obtained via geometry optimization using EMFT, in comparison to the corresponding values obtained using both the low-level and high-level DFT methods. The rows of the table are grouped into distances between atoms that are within the high-level region of the EMFT description (top unshaded block), distances between atoms that span the high- and low-level regions (shaded block), and distances between atoms that are within the low-level region of the EMFT description (bottom unshaded block). Corresponding tables for Catalysts 2–4 are provided in the Supporting Information.

The general expectation of EMFT is for bonds within the high-level subsystem to be described at the quality of the high-level DFT; this is largely borne out in Table 1 by the fact that the difference between the EMFT and high-level DFT bond lengths (EMFT – B3LYP) for atoms within the high-level region are smaller than the corresponding difference between EMFT and the low-level DFT bond lengths (EMFT – PBE). Similarly, the there is an expectation for bonds within the low-level subsystem to be described by EMFT at the quality of the low-level DFT; this is again supported by the data in Table 1 by the fact that the difference between the EMFT and low-level DFT bond lengths (EMFT – PBE) for atoms within the low-level region are smaller than the corresponding difference between EMFT and the high-level DFT bond lengths (EMFT – B3LYP). For bonds that span the high- and low-level subsystems, it is seen in the table that these distances are generally more consistent with the description of the low-level DFT theory, as is expected; nonetheless, we find some cases, like the Ti–N bond length, where the description of the atoms spanning the high- and low system deviates substantially from both the high- and low-level DFT methods.

Figure 9 summarizes the results in Table 1 and generalizes them to Catalysts 2–4. In Figure 9a, we plot the root-mean-square-error (RMSE) for the difference between EMFT-optimized bond lengths and either high-level or low-level DFT-optimized bond lengths for atoms contained within the high-level region of the minimal EMFT partitioning. In Figure

Table 1: For Catalyst 1, bond lengths are compared between EMFT ((B3LYP/Def2-SVP)-in-(PBE/6-31G)), high-level DFT (B3LYP/Def2-SVP), and low-level DFT (PBE/6-31G). The minimal subsystem partitioning is used for EMFT (Figure 3, $X = 1$). Columns are grouped according to bonds located within the high-level subsystem (top unshaded block), across the high- and low-level subsystems (shaded block), or within the low-level subsystem (bottom unshaded block). Duplicate names for atoms are given superscript indexing for differentiation. The bond length computed by EMFT, the difference between the EMFT and PBE-calculated bond lengths (EMFT – PBE), and the difference between the EMFT and B3LYP-calculated bond lengths (EMFT – B3LYP) are presented.

First Atom	Second Atom	EMFT (Å)	EMFT – PBE (Å)	EMFT – B3LYP (Å)
Ti	C(n-Pr)^1	2.071	−0.010	−0.005
C(n-Pr)^1	C(n-Pr)^2	1.513	−0.012	−0.001
Ti	C(ring)^1	2.229	−0.013	−0.002
Ti	C(ring)^2	2.362	0.005	0.010
Ti	C(ring)^3	2.557	0.023	0.065
Ti	C(ring)^4	2.515	0.021	0.068
Ti	C(ring)^5	2.281	−0.009	0.018
Ti	N	1.790	−0.102	−0.104
N	Si	1.899	0.012	0.085
N	C(t-Bu)	1.510	0.001	0.015
Si	C(ring)^1	1.927	−0.004	0.018

9b, we present the corresponding results for bond lengths involving atoms that lie within the low-level region of the EMFT partitioning. For Catalyst 1, these results are obtained from the data reported in Table 1, and for Catalysts 2–4, the data are obtained from the corresponding tables in the Supporting Information. It is clear that for all four catalysts, the EMFT-optimized geometries yield a description of atoms within the high-level region that is more consistent with the high-level DFT description (panel a), whereas the atoms with low-level region are more closely described at the level of the low-level DFT (panel b). These results clearly illustrate that EMFT provides improved accuracy in the high-level region while describing the remainder of the system at the quality of the low-level DFT theory.

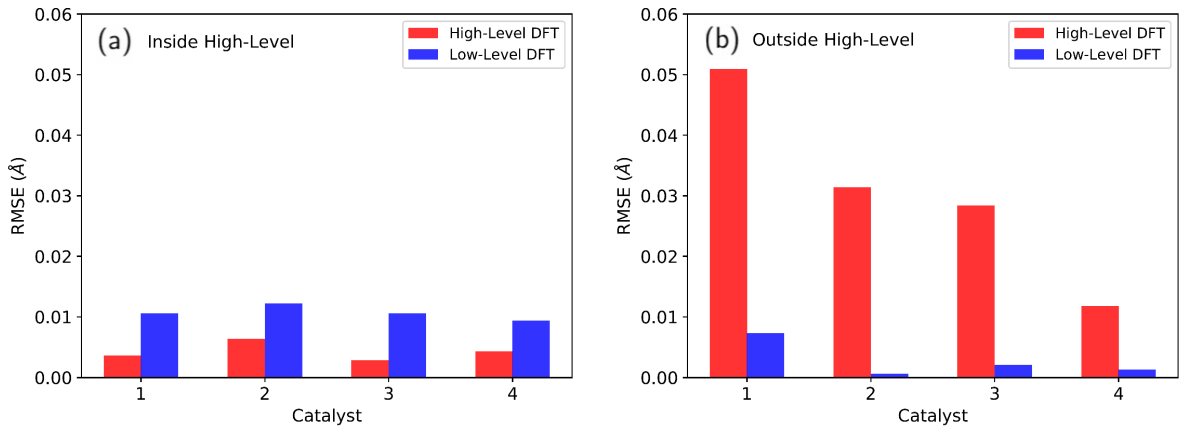

Figure 9: Root-mean-square error (RMSE) of bond lengths between EMFT and full-DFT geometry optimized structures for representative bonds that are (**a**) inside the high-level subsystem or (**b**) outside the high-level subsystem. The minimal subsystem partitioning is used for EMFT (Figure 3, $X = 1$).

Cost Analysis

The preceding results have shown that even with the minimal number of atoms in the high-level region (partitioning 1), EMFT provides a description across all four catalysts considered here that is within chemical accuracy for substrate binding, reliable for resting-state conformer stability ranking, and yields optimized geometries that are consistent with the high-level DFT method around the catalyst active site. Furthermore, as has been emphasized in previous work,[23,28] the use of EMFT brings substantial reductions in computational cost in comparison to using the high-level DFT method for the full system. The reduced cost of EMFT comes from both the reduced size of the basis set in the low-level region, as well as the lower cost of evaluating the low-level DFT exchange correlation function for the atoms in the low-level region. Specifically, in the current applications, the use of EMFT reduced the need for evaluating exact exchange contributions to only the atoms within the high-level subsystem.

Table 2 compares timings for EMFT ((B3LYP/Def2-SVP)-in-(PBE/6-31G)) in comparison to high-level DFT (B3LYP/Def2-SVP) and low-level DFT (PBE/6-31G) applied to the full system. In all cases, EMFT is performed using the minimal partitioning (partitioning

1). For each of the catalysts, timings are reported for the energy calculation such that 11 atoms are described in the high-level region (e.g. metal, propyl side-chain). All calculations were done on 16-core Intel Skylake dual-CPUs with a clock speed of 2.1 GHz.

As is seen from Table 2, EMFT yields a cost reduction that ranges from a factor of 4 for the smallest catalyst (Catalyst 1) to a factor of ∼20 for the largest catalysts (Catalysts 2 and 3). In general, the EMFT cost is only slightly increased relative to that for the low-level DFT method. Furthermore, the number of self-consistent field iterations needed for EMFT is similar to the standard DFT methods. These results, in combination with the previously shown benchmarks of EMFT accuracy, illustrate that the method preserves accuracy of the high-level DFT method while providing vast reductions in computational cost.

Table 2: For the resting state structures of Catalysts 1–4, energy calculation timings for EMFT ((B3LYP/Def2-SVP)-in-(PBE/6-31G)) in comparison to high-level DFT (B3LYP/Def2-SVP) and low-level DFT (PBE/6-31G) applied to the full system. EMFT calculations employ the minimal high-level subsystem partitioning. Timings reported using 16-core Intel Skylake dual-CPUs with a clock speed of 2.1 GHz.

Catalyst	Settings	SCF Time (s)	Cycles	Total SCF Time (s)
	High-Level DFT	1.0	18	18.6
1	**EMFT**	**0.4**	**21**	**8.4**
	Low-Level DFT	0.3	22	5.7
	High-Level DFT	33.1	20	662.8
2	**EMFT**	**1.4**	**20**	**27.9**
	Low-Level DFT	1.1	20	22.6
	High-Level DFT	25.1	19	477.8
3	**EMFT**	**1.3**	**22**	**28.3**
	Low-Level DFT	1.1	25	26.5
	High-Level DFT	13.3	19	251.9
4	**EMFT**	**0.9**	**19**	**18.0**
	Low-Level DFT	0.8	20	14.8

Application of EMFT for QM/MM Simulations

To illustrate the applicability of EMFT for the simulation of condensed phase reactions associated with these homogeneous catalysts, we present EMFT/MM simulations (i.e., QM/MM simulations with EMFT used for the QM region) of ethylene binding to Catalyst 1. We model the ion-pairing of this cationic catalyst with four different counterions ranging from small, strongly-coordinating anions Cl^- and BF_4^- to sterically-bulky, weakly-coordinating anions $CH_3B(C_6F_5)_3^-$ and $B(C_6F_5)_4^-$. Particular focus is given to the way in which the cationic catalyst interacts with counterions of varying size, given the crucial role that the counterion plays in catalyst efficiency.[69]

EMFT/MM simulations are performed using EMFT ((B3LYP-D3/Def2-SVP)-in-(PBE-D3/6-31G)) with the minimal high-level subsystem partitioning and using the D3 dispersion correction in both the high- and low-level regions.[70] The ethylene-bound Catalyst 1, with 61 atoms, is included in the EMFT region while the counterions and solvent (193–196 toluene molecules) are treated within the MM region, as illustrated in Figure 10. Full calculation details are provided in the Computational Methods section.

As a demonstration of robustness, Figure 11 illustrates the energy conservation of microcanonical EMFT/MM trajectories for each of the four considered counterions. In each case, we show that there is minimal drift in the total energy, which is plotted relative to the average kinetic energy for the system of the entire trajectory. The small fluctuations and drift of the total energy in these plots over 30 ps indicates the good energy conservation of the EMFT/MM trajectories.

We qualitatively assess the strength of the interaction between the cationic catalyst and the anionic counterion using the radial distribution function (RDF) for the two species. Specifically, Figure 12 plots the RDF with respect to the distance between the Ti atom of Catalyst 1 and the center-of-mass of each of the four considered counterions from separate EMFT/MM simulations.

It is clear that the EMFT/MM simulations lead to qualitatively different RDF profiles

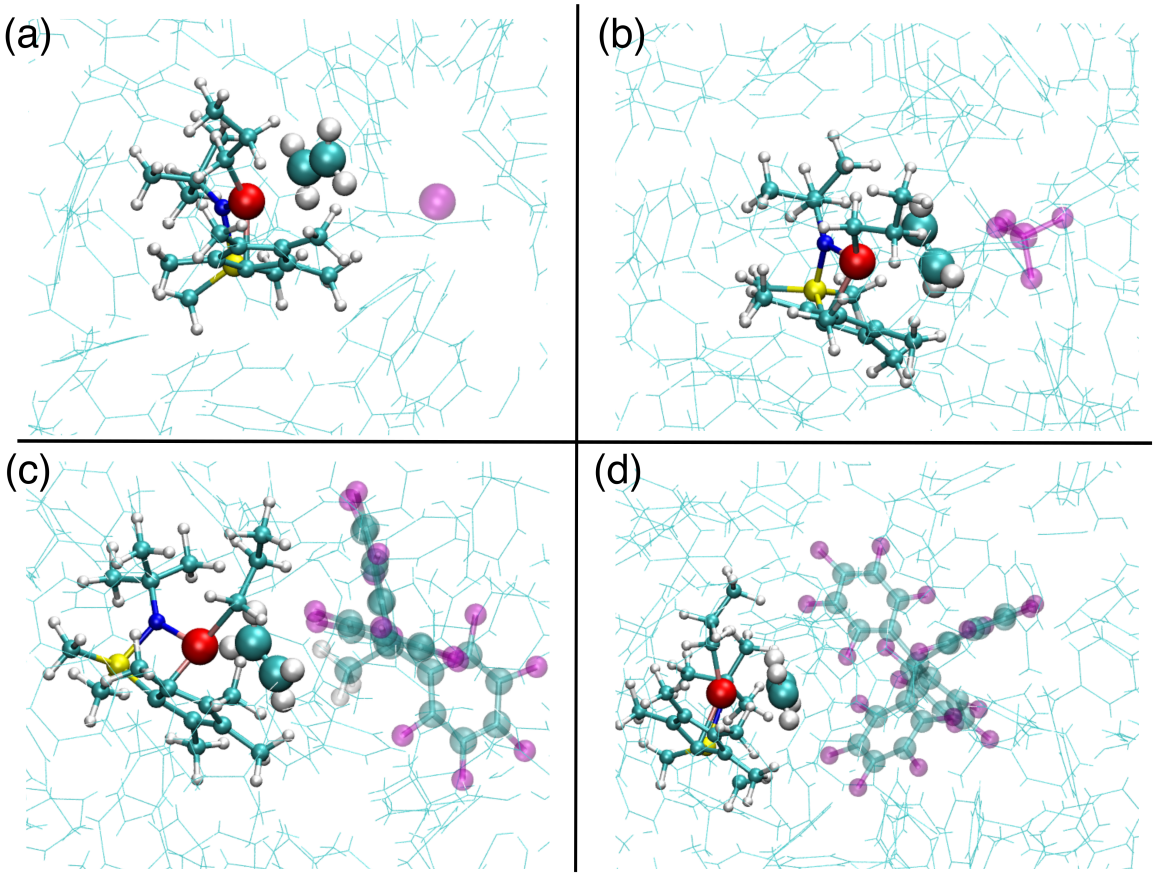

Figure 10: Snapshots of the QM and MM subsystems used in the EMFT/MM simulations. Catalyst 1 complex is presented as a balls-and-stick model, with Ti, Si, N, C, and H atoms colored in red, yellow, blue, cyan, and white, respectively. Toluene molecules (solvent) are shown using blue lines. From a–d respectively, the counteranions of interest, Cl^-, BF_4^-, $CH_3B(C_6F_4)_3^-$, and $B(C_6F_5)_4^-$, are depicted with a transparent ball-and-stick structure. Each simulation is solvated in toluene with 193 to 196 molecules in a periodic simulation cell.

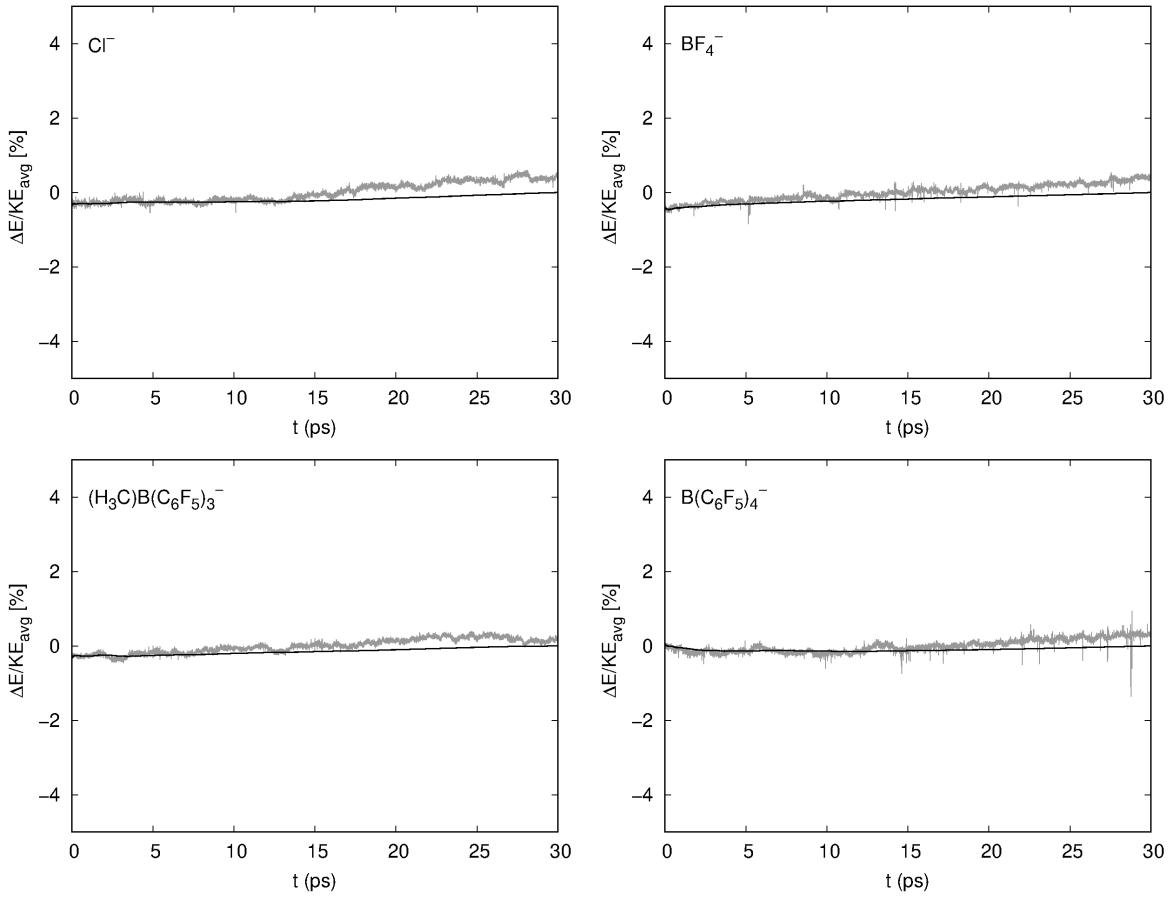

Figure 11: Energy conservation plots for EMFT/MM trajectories for Catalyst 1 with solvent and various counterions (indicated in each panel) in the NVE ensemble. The gray line indicates $(E(t) - E_{\mathrm{avg}})/(\mathrm{KE}_{\mathrm{avg}})$, while the black line indicates the cumulative average of the same quantity.

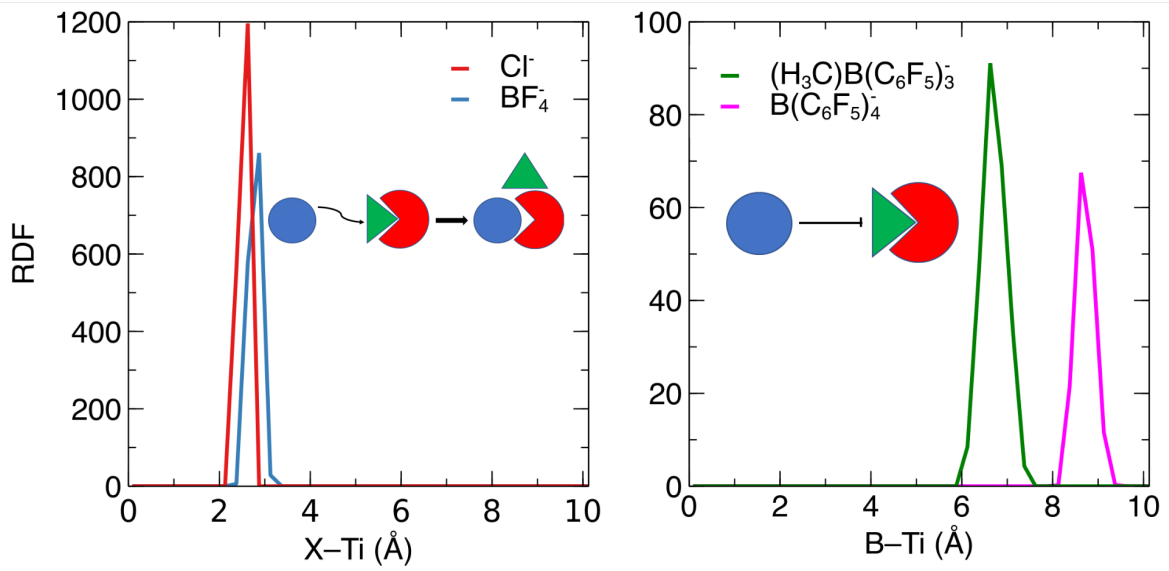

Figure 12: RDF for the distance between Catalyst 1 and its counterion in the four EMFT/MM simulations computed between 15–30 ps.(**a**) Close contact between the small counterions (blue circle) and the metal binding site leads to dissociation of ethylene (green triangle) from the catalyst (red semicircle). (**b**) Ethylene remains bound to the metal binding site in the presence of bulky counterions.

for the smaller (Figure 12a) versus bulkier (Figure 12b) counteranions. The small, strongly coordinating counterions chloride (Cl^-) and tetrafluoroborate (BF_4^-) are on average more closely associated with Catalyst 1 than the bulkier counterions. Specifically Cl^- and BF_4^- counteranions are located at $\sim$ 2.5 Å from the Ti atom, which is 4 Å closer than that of $CH_3B(C_6F_5)_3^-$ and $B(C_6F_5)_4^-$.

The close binding of the chloride and tetrafluoroborate ions to the catalyst has direct consequences for the reactivity of the catalyst in solution. In the EMFT/MM simulations performed with these smaller counterions, the ethylene substrate that is originally bound to the catalyst is displaced from the binding site within 10 ps, driven by the formation of the close contact of these counterions with the Ti atom. Schematically, this is shown in Figure 12a cartoon with the counterion (blue circle) displacing the substrate (green triangle) from the catalyst (red semicircle) binding site. Conversely, in the EMFT/MM simulations involving the larger counterions $CH_3B(C_6F_5)_3^-$ and $B(C_6F_5)_4^-$, the ethylene substrate remains coordinated to the Ti atom of Catalyst 1. Experimentally, it is also known that the

toluene solvent will compete with the ethylene substrate for binding, although this not seen on the timescales of these simulations.[71] The simulations indicate that olefin binding (Step 2, Figure 1) is strongly influenced by the strength of the interaction between the counterion and metal complex. The results presented here are consistent with previous literature demonstrating that bulkier counteranions increase the efficiency of the catalyst by binding more weakly to the catalyst, thus promoting monomer binding and polymerization at the cationic active site.[62,69,72,73]

Conclusion

We have developed a framework for combined EMFT and QM/MM MD simulations. Our benchmarks indicate that for the wide range Group (IV) transition-metal polyolefin catalysts, using a minimal high-level region for EMFT reproduces the energetic and structural properties obtained by high-level DFT on the entire system. According to the timing data provided in Table 2, EMFT is able to reduce the cost of DFT calculations from a factor of 4 up to a factor of 20 per SCF iteration while maintaining the accuracy of the high-level DFT (hybrid functional). EMFT/MM simulations of counteranion binding to the cationic catalyst demonstrate energy conservation within the range expected given the truncated treatment of electrostatics, and provide insights into the nature of counteranion binding as a function of counteranion size. Our results indicate that ethylene binding to the activated catalyst is significantly influenced by the interaction between the counterion and metal complex. Close contact between the counterion and metal complex (i.e. Cl^- and BF_4^-) leads to dissociation of ethylene from the catalyst binding site.

Understanding the detailed role of the solvent and counterion environment is critical for reliable prediction of catalytic activity, and hence for the design of new catalysts. While conventional QM/MM simulations using hybrid DFT in the QM region are often unaffordable, the EMFT embedding scheme provides the desired level of accuracy at greatly reduced com-

putational cost, by tuning in the exact exchange treatment to just a small number of atoms in the immediate vicinity of the active transition-metal center. This is a key step on the path towards widespread use of QM/MM simulation for discovery of new transition-metal catalysts, both for polyolefin catalysis, and more widely.

Acknowledgement

This work was carried out with financial support within the University Partnership Initiative from the Dow Chemical Company. This material is based upon work supported by the National Science Foundation Graduate Research Fellowship under Grant No. DGE–1144469.

Supporting Information

The attached compressed folders contain the following data: (1) XYZ coordinate files for the resting state and monomer-bound catalyst structures, (2) DFT-optimized structures of the Catalyst 3 conformers, (3) EMFT-optimized structures of the Catalyst 3 conformers, and (4) GROMACS files for the QM/MM study.

This information is available free of charge via the Internet at http://pubs.acs.org.

Authorship

L.C. and J.L. are co-first authors.

References

(1) Poree, C.; Schoenebeck, F. A Holy Grail in Chemistry: Computational Catalyst Design: Feasible or Fiction? *Acc. Chem. Res.* **2017**, *50*, 605–608.

(2) Busico, C. Ziegler-Natta catalysis: Forever young. *MRS Bull.* **2013**, *38*, 224–228.

(3) Chen, C. Designing catalysts for olefin polymerization and copolymerization: Beyond electronic and steric tuning. *Nat. Rev. Chem.* **2018**, *2*, 6–14.

(4) Warshel, A.; Levitt, M. Theoretical studies of enzymic reactions: Dielectric, electrostatic and steric stabilization of the carbonium ion in the reaction of lysozyme. *J. Mol. Biol.* **1976**, *103*, 227–249.

(5) Warshel, A.; Karplus, M. Calculation of ground and excited state potential surfaces of conjugated molecules. I. Formulation and parametrization. *J. Am. Chem. Soc.* **1972**, *94*, 5612–5625.

(6) Woods, C. J.; Shaw, K. E.; Mulholland, A. J. Combined Quantum Mechanics/Molecular Mechanics (QM/MM) Simulations for Protein–Ligand Complexes: Free Energies of Binding of Water Molecules in Influenza Neuraminidase. *J. Phys. Chem. B* **2014**, *119*, 997–1001.

(7) Gong, W.; Wu, R.; Zhang, Y. Thiol Versus Hydroxamate as Zinc Binding Group in HDAC Inhibition: An Ab Initio QM/MM Molecular Dynamics Study. *J. Comput. Chem.* **2015**, *36*, 2228–2235.

(8) Ugur, I.; Marion, A.; Aviyente, V.; Monard, G. Why Does Asn71 Deamidate Faster Than Asn15 in the Enzyme Triosephosphate Isomerase? Answers from Microsecond Molecular Dynamics Simulation and QM/MM Free Energy Calculations. *Biochemistry* **2015**, *54*, 1429–1439.

(9) David, R.; Jamet, H.; Nivière, V.; Moreau, Y.; Milet, A. Iron Hydroperoxide Intermediate in Superoxide Reductase: Protonation or Dissociation First? MM Dynamics and QM/MM Metadynamics Study. *J. Chem. Theory Comput.* **2017**, *13*, 2987–3004.

(10) Ranaghan, K. E.; Morris, W. G.; Masgrau, L.; Senthilkumar, K.; Johannissen, L. O.; Scrutton, N. S.; Harvey, J. N.; Manby, F. R.; Mulholland, A. J. Ab Initio QM/MM

Modeling of the Rate-Limiting Proton Transfer Step in the Deamination of Tryptamine by Aromatic Amine Dehydrogenase. *J. Phys. Chem. B* **2017**, *121*, 9785–9798.

(11) Steinmann, C.; Olsson, M. A.; Ryde, U. Relative Ligand-Binding Free Energies Calculated from Multiple Short QM/MM MD Simulations. *J. Chem. Theory Comput.* **2018**, *14*, 3228–3237.

(12) Ortuño, M. A.; Vidossich, P.; Ujaque, G.; Conejero, S.; Lledós, A. Solution dynamics of agostic interactions in T-shaped Pt(II) complexes from ab initio molecular dynamics simulations. *Dalton Trans.* **2013**, *42*, 12165–12172.

(13) Shen, L.; Yang, W. Quantum Mechanics/Molecular Mechanics Method Combined with Hybrid All-Atom and Coarse-Grained Model: Theory and Application on Redox Potential Calculations. *J. Chem. Theory Comput.* **2016**, *12*, 2017–2027.

(14) Wood, G. P. F.; Sreedhara, A.; Moore, J. M.; Wang, J.; Trout, B. L. Mechanistic Insights into Radical-Mediated Oxidation of Tryptophan from ab Initio Quantum Chemistry Calculations and QM/MM Molecular Dynamics Simulations. *J. Phys. Chem. A* **2016**, *120*, 2926–2939.

(15) Zvereva, E. E.; Katsyuba, S. A.; Dyson, P. J.; Aleksandrov, A. V. Solvation of Palladium Clusters in an Ionic Liquid: A QM/MM Molecular Dynamics Study. *J. Phys. Chem. C* **2016**, *120*, 4596–4604.

(16) Hofer, T. S.; Hünenberger, P. H. Absolute proton hydration free energy, surface potential of water, and redox potential of the hydrogen electrode from first principles: QM/MM MD free-energy simulations of sodium and potassium hydration. *J. Chem. Phys.* **2018**, *148*, 222814.

(17) Manby, F.; Stella, M.; Goodpaster, J.; Miller, T. F., III A Simple, Exact Density-Functional-Theory Embedding Scheme. *J. Chem. Theory Comput.* **2012**, *8*, 2564–2568.

(18) Lee, S. J. R.; Welborn, M.; Manby, F. R.; Miller, T. F., III Projection-Based Wavefunction-in-DFT Embedding. *Acc. Chem. Res.* **2019**, *52*, 1359–1368.

(19) Chulhai, D.; Goodpaster, J. Projection-Based Correlated Wave Function in Density Functional Theory Embedding for Periodic Systems. *J. Chem. Theory Comput.* **2018**, *14*, 1928–1942.

(20) Bennie, S.; van der Kamp, M.; Pennifold, R.; Stella, M.; Manby, F.; Mulholland, A. A Projector-Embedding Approach for Multiscale Coupled-Cluster Calculations Applied to Citrate Synthase. *J. Chem. Theory Comput.* **2016**, *12*, 2689–2697.

(21) Zhang, X.; Bennie, S.; van der Kamp, M.; Glowacki, D.; Manby, F. R.; Mulholland, A. J. Multiscale analysis of enantioselectivity in enzyme-catalysed 'lethal synthesis' using projector-based embedding. *R. Soc. Open Sci.* **2018**, *5*, 171390.

(22) Barnes, A.; Kaminski, J.; Borodin, O.; Miller, T. F., III Ab Initio Characterization of the Electrochemical Stability and Solvation Properties of Condensed-Phase Ethylene Carbonate and Dimethyl Carbonate Mixtures. *J. Phys. Chem. C* **2015**, *119*, 3865–3880.

(23) Fornace, M. E.; Lee, J.; Miyamoto, K.; Manby, F. R.; Miller, T. F., III Embedded Mean-Field Theory. *J. Chem. Theory Comput.* **2015**, *11*, 568–580.

(24) Ding, F.; Manby, F. R.; Miller, T. F., III Embedded Mean-Field Theory with Block-Orthogonalized Partitioning. *J. Chem. Theory Comput.* **2017**, *13*, 1605–1615.

(25) Bakowies, D.; Thiel, W. Hybrid Models for Combined Quantum Mechanical and Molecular Mechanical Approaches. *J. Phys. Chem.* **1996**, *100*, 10580–10594.

(26) Dapprich, S.; KomÃąromi, I.; Byun, K.; Morokuma, K.; Frisch, M. J. A new ONIOM implementation in Gaussian98. Part I. The calculation of energies, gradients, vibrational frequencies and electric field derivatives1Dedicated to Professor Keiji Morokuma in celebration of his 65th birthday.1. *J. Mol. Struct.:THEOCHEM* **1999**, *461-462*, 1 – 21.

(27) Vreven, T.; Byun, K. S.; KomÃąromi, I.; Dapprich, S.; Montgomery, J. A.; Morokuma, K.; Frisch, M. J. Combining Quantum Mechanics Methods with Molecular Mechanics Methods in ONIOM. *J. Chem. Theory Comput.* **2006**, *2*, 815–826, PMID: 26626688.

(28) Jiang, H.; Kammler, M.; Ding, F.; Dorenkamp, Y.; Manby, F. R.; Wodtke, A. M.; Miller, T. F., III; Kandratsenka, A.; Bünermann, O. Imaging covalent bond formation by H atom scattering from graphene. *Science* **2019**, *364*, 379–382.

(29) Lee, S. J.; Miyamoto, K.; Ding, F.; Manby, F. R.; Miller, T. F. Density-based errors in mixed-basis mean-field electronic structure, with implications for embedding and QM/MM methods. *Chem. Phys. Lett.* **2017**, *683*, 375 – 382, Ahmed Zewail (1946-2016) Commemoration Issue of Chemical Physics Letters.

(30) Ding, F.; Tsuchiya, T.; Manby, F. R.; Miller, T. F. Linear-Response Time-Dependent Embedded Mean-Field Theory. *J. Chem. Theory Comput.* **2017**, *13*, 4216–4227, PMID: 28783359.

(31) Kaminsky, W. Trends in Polyolefin Chemistry. *Macromol. Chem. Phys.* **2008**, *209*, 459–466.

(32) Rappé, A. K.; Skiff, W. M.; Casewit, C. J. Modeling Metal-Catalyzed Olefin Polymerization. *Chem. Rev.* **2000**, *100*, 1435–1456.

(33) Coates, G. W. Precise Control of Polyolefin Stereochemistry Using Single-Site Metal Catalysts. *Chem. Rev.* **2000**, *100*, 1223–1252.

(34) Landis, C. R.; Sillars, D. R.; Batterton, J. M. Reactivity of Secondary Metallocene Alkyls and the Question of Dormant Sites in Catalytic Alkene Polymerization. *J. Am. Chem. Soc.* **2004**, *126*, 8890–8891.

(35) Woo, T. K.; Margl, P. M.; Ziegler, T.; Blöchl, P. E. Static and ab Initio Molecular Dynamics Study of the Titanium(IV)-Constrained Geometry Catalyst ($CpSiH_2NH$)Ti-R^+. 2. Chain Termination and Long Chain Branching. *Organometallics* **1997**, *16*, 3454–3468.

(36) Margl, P. M.; Deng, L.; Ziegler, T. Cobalt(II) Imino Pyridine Assisted Ethylene Polymerization: A Quantum-Mechanical/Molecular-Mechanical Density Functional Theory Investigation. *Organometallics* **1999**, *18*, 5701–5708.

(37) Lanza, G.; Fragalà, I. L.; Marks, T. J. Ligand Substituent, Anion, and Solvation Effects on Ion Pair Structure, Thermodynamic Stability, and Structural Mobility in "Constrained Geometry" Olefin Polymerization Catalysts: an Ab Initio Quantum Chemical Investigation. *J. Am. Chem. Soc.* **2000**, *122*, 12764–12777.

(38) Lanza, G.; Fragalà, I. L.; Marks, T. J. Energetic, Structural, and Dynamic Aspects of Ethylene Polymerization Mediated by Homogeneous Single-Site "Constrained Geometry Catalysts" in the Presence of Cocatalyst and Solvation: An Investigation at the ab Initio Quantum Chemical Level. *Organometallics* **2002**, *21*, 5594–5612.

(39) Solans-Monfort, X.; Clot, E.; Copéret, C.; Eisenstein, O. Understanding Structural and Dynamic Properties of Well-Defined Rhenium-Based Olefin Metathesis Catalysts, Re(≡CR)(=CHR)(X)(Y), from DFT and QM/MM Calculations. *Organometallics* **2005**, *24*, 1586–1597.

(40) Yang, S.-Y.; Ziegler, T. Combined Car–Parrinello QM/MM Dynamic Study on the Propagation and Termination Steps of Ethylene Polymerization Catalyzed by [$Cp_2ZrR(\mu$-Me)$B(C_6F_5)_3$] (R = Me, Pr). *Organometallics* **2006**, *25*, 887–900.

(41) Devore, D. D.; Timmers, F. J.; Hasha, D. L.; Rosen, R. K.; Marks, T. J.; Deck, P. A.; Stern, C. L. Constrained-Geometry Titanium(II) Diene Complexes. Structural Diversity and Olefin Polymerization Activity. *Organometallics* **1995**, *14*, 3132–3134.

(42) Woo, T. K.; Margl, P. M.; Lohrenz, J. C. W.; Blöchl, P. E.; Ziegler, T. Combined Static and Dynamic Density Functional Study of the Ti(IV) Constrained Geometry Catalyst ($CpSiH_2NH$)TiR^+. 1. Resting States and Chain Propagation. *J. Am. Chem. Soc.* **1996**, *118*, 13021–13030.

(43) Zhou, Z.; Stevens, J. C.; Klosin, J.; Kümmerle, R.; Qiu, X.; Redwine, D.; Cong, R.; Taha, A.; Mason, J.; Winniford, B.; Chauvel, P.; Montañez, N. NMR Study of Isolated 2,1-Inverse Insertion in Isotactic Polypropylene. *Macromolecules* **2009**, *42*, 2291–2294.

(44) Arriola, D. J.; Carnahan, E. M.; Hustad, P. D.; Kuhlman, R. L.; Wenzel, T. T. Catalytic Production of Olefin Block Copolymers via Chain Shuttling Polymerization. *Science* **2006**, *312*, 714–719.

(45) Becke, A. D. Density-functional thermochemistry. III. The role of exact exchange. *J. Chem. Phys.* **1998**, *98*, 5648–5652.

(46) Lee, C.; Yang, W.; Parr, R. G. Development of the Colle-Salvetti correlation-energy formula into a functional of the electron density. *Phys. Rev. B* **1988**, *37*, 785–789.

(47) Vosko, S. H.; Wilk, L.; Nusair, M. Accurate spin-dependent electron liquid correlation energies for local spin density calculations: A critical analysis. *Can. J. Phys.* **2011**, *58*, 1200–1211.

(48) Stephens, P. J.; Devlin, F. J.; Chabalowski, C. F.; Frisch, M. J. Ab initio calculation of vibrational absorption and circular dichroism spectra using density functional force fields. *J. Phys. Chem.* **1994**, *98*, 11623–11627.

(49) Ricca, A.; Bauschlicher, C. W. J. Successive Binding Energies of $Fe(CO)_5^+$. *J. Phys. Chem.* **1994**, *98*, 12899–12903.

(50) Musaev, D. G.; Morokuma, K. Structure, Stability, and Bonding of Transition-

Metal–Boryl Complexes. A Molecular Orbital Study. *J. Phys. Chem.* **1996**, *100*, 6509–6517.

(51) Froese, R. D. J.; Musaev, D. G.; Morokuma, K. Theoretical Study of Substituent Effects in the Diimine–M(II) Catalyzed Ethylene Polymerization Reaction Using the IMOMM Method. *J. Am. Chem. Soc.* **1998**, *120*, 1581–1587.

(52) Froese, R. D. J.; Musaev, D. G.; Morokuma, K. Theoretical Studies of the Factors Controlling Insertion Barriers for Olefin Polymerization by the Titanium-Chelating Bridged Catalysts. A Search for More Active New Catalysts. *Organometallics* **1999**, *18*, 373–379.

(53) Perdew, J. P.; Burke, K.; Ernzerhof, M. Generalized Gradient Approximation Made Simple. *Phys. Rev. Lett.* **1996**, *77*, 3865–3868.

(54) Manby, F.; Miller, T.; Bygrave, P.; Ding, F.; Dresselhaus, T.; Batista-Romero, F.; Buccheri, A.; Bungey, C.; Lee, S.; Meli, R.; Miyamoto, K.; Steinmann, C.; Tsuchiya, T.; Welborn, M.; Wiles, T. entos: A Quantum Molecular Simulation Package. **2019**,

(55) Vosko, S. H.; Wilk, L.; Nusair, M. Accurate spin-dependent electron liquid correlation energies for local spin density calculations: a critical analysis. *Can. J. Phys.* **1980**, *58*, 1200–1211.

(56) Grimme, S.; Bannwarth, C.; Shushkov, P. A Robust and Accurate Tight-Binding Quantum Chemical Method for Structures, Vibrational Frequencies, and Noncovalent Interactions of Large Molecular Systems Parametrized for All spd-Block Elements (Z = 1âĂŞ86). *J. Chem. Theory Comput.* **2017**, *13*, 1989–2009.

(57) Berendsen, H. J. C.; van der Spoel, D.; van Drunen, R. GROMACS: A message-passing parallel molecular dynamics implementation. *Comput. Phys. Commun.* **1995**, *91*, 43–56.

(58) Jorgensen, W. L.; Tirado-Rives, J. Potential energy functions for atomic-level simulations of water and organic and biomolecular systems. *J. Proc. Natl. Acad. Sci.* **2005**, *102*, 6665–6670.

(59) Caleman, C.; van Maaren, P. J.; Hong, M.; Hub, J. S.; Costa, L. T.; van der Spoel, D. Force Field Benchmark of Organic Liquids: Density, Enthalpy of Vaporization, Heat Capacities, Surface Tension, Isothermal Compressibility, Volumetric Expansion Coefficient, and Dielectric Constant. *J. Chem. Theory Comput.* **2012**, *8*, 61–74, PMID: 22241968.

(60) virtualchemistry. `http://virtualchemistry.org/`.

(61) Mulliken, R. S. Electronic Population Analysis on LCAOâĂŞMO Molecular Wave Functions. I. *J. Chem. Phys.* **1955**, *23*, 1833–1840.

(62) Rowley, C. N.; Woo, T. K. Counteranion Effects on the Zirconocene Polymerization Catalyst Olefin Complex from QM/MM Molecular Dynamics Simulations. *Organometallics* **2011**, *30*, 2071–2074.

(63) van Gunsteren, W. F.; Berendsen, H. J. C.; Rullmann, J. A. C. Inclusion of reaction fields in molecular dynamics. Application to liquid water. *Faraday Discuss Chem Soc.* **1978**, *66*, 58–70.

(64) Hess, B.; Bekker, H.; Berendsen, H. J. C.; Fraaije, J. G. E. M. LINCS: A linear constraint solver for molecular simulations. *J. Comput. Chem.* **1997**, *18*, 1463–1472.

(65) Evans, D. J.; Holian, B. L. The Nosé-Hoover thermostat. *J. Chem. Phys.* **1985**, *83*, 4069–4074.

(66) Parrinello, M.; Rahman, A. Polymorphic transitions in single crystals: A new molecular dynamics method. *J. Appl. Phys.* **1981**, *52*, 7182–7190.

(67) Lindahl, E.; Hess, B.; van der Spoel, D. GROMACS 3.0: a package for molecular simulation and trajectory analysis. *J. Mol. Model.* **2001**, *7*, 306–317.

(68) Malinoski, J.; White, P.; Brookhart, M. Structural Characterization of [κ2-(t-Bu)$_2$PCH$_2$PC(O)C$_6$PH$_5$P]PdMe(η^2P-C$_2$H$_4$)$^+$BAr$_4$$^-$: A Model for the Catalyst Resting State for Ethylene Polymerization. *Organometallics* **2003**, *22*, 621–623.

(69) Chen, Y.-X.; Stern, C. L.; Yang, S.; Marks, T. J. Organo-Lewis Acids As Cocatalysts in Cationic Metallocene Polymerization Catalysis. Unusual Characteristics of Sterically Encumbered Tris(perfluorobiphenyl)borane. *J. Am. Chem. Soc.* **1996**, *118*, 12451–12452.

(70) Grimme, S.; Antony, J.; Ehrlich, S.; Krieg, H. A consistent and accurate ab initio parametrization of density functional dispersion correction (DFT-D) for the 94 elements H-Pu. *The Journal of Chemical Physics* **2010**, *132*, 154104.

(71) Collins, R. A.; Russell, A. F.; Mountford, P. Group 4 metal complexes for homogeneous olefin polymerisation: a short tutorial review. *Appl. Petrochem. Res.* **2015**, *5*, 153–171.

(72) Roberts, J. A. S.; Chen, M.-C.; Seyam, A. M.; Li, L.; Zuccaccia, C.; Stahl, N. G.; Marks, T. J. Diverse Stereocontrol Effects Induced by Weakly Coordinating Anions. Stereospecific Olefin Polymerization Pathways at Archetypal Cs- and C1-Symmetric Metallocenium Catalysts Using Mono- and Polynuclear Halo-perfluoroarylmetalates as Cocatalysts. *J. Am. Chem. Soc.* **2007**, *129*, 12713–12733.

(73) Riddlestone, I. M.; Kraft, A.; Schaefer, J.; Krossing, I. Taming the Cationic Beast: Novel Developments in the Synthesis and Application of Weakly Coordinating Anions. *Angew. Chem.* **2018**, *57*, 13982–14024.

Graphical TOC Entry